Boundary-Layer Meteorol (2013) 148:51–72
DOI 10.1007/s10546-013-9803-4

ARTICLE

Surface Temperature and Surface-Layer Turbulence in a Convective Boundary Layer

Anirban Garai · Eric Pardyjak · Gert-Jan Steeneveld · Jan Kleissl

Received: 2 August 2012 / Accepted: 29 January 2013 / Published online: 1 March 2013

Abstract Previous laboratory and atmospheric experiments have shown that turbulence influences the surface temperature in a convective boundary layer. The main objective of this study is to examine land-atmosphere coupled heat transport mechanism for different stability conditions. High frequency infrared imagery and sonic anemometer measurements were obtained during the boundary layer late afternoon and sunset turbulence (BLLAST) experimental campaign. Temporal turbulence data in the surface-layer are then analyzed jointly with spatial surface-temperature imagery. The surface-temperature structures (identified using surface-temperature fluctuations) are strongly linked to atmospheric turbulence as manifested in several findings. The surface-temperature coherent structures move at an advection speed similar to the upper surface-layer or mixed-layer wind speed, with a decreasing trend with increase in stability. Also, with increasing instability the streamwise surface-temperature structure size decreases and the structures become more circular. The sequencing of surface- and air-temperature patterns is further examined through conditional averaging. Surface heating causes the initiation of warm ejection events followed by cold sweep events that result in surface cooling. The ejection events occur about 25 % of the time, but account for 60–70 % of the total sensible heat flux and cause fluctuations of up to 30 % in the ground heat flux. Cross-correlation analysis between air and surface temperature confirms the validity of a scalar footprint model.

Electronic supplementary material The online version of this article (doi:10.1007/s10546-013-9803-4) contains supplementary material, which is available to authorized users.

A. Garai · J. Kleissl (✉)
Department of Mechanical and Aerospace Engineering, University of California, 9500 Gilman Drive, EBUII–580, La Jolla, San Diego, CA 92093-0411, USA
e-mail: jkleissl@ucsd.edu

E. Pardyjak
Department of Mechanical Engineering, University of Utah, Salt Lake City, USA

G.-J. Steeneveld
Meteorology and Air Quality, Wageningen University, Wageningen, The Netherlands

Keywords Atmospheric surface layer · Convective boundary layer · Infra-red imagery · Surface-layer plumes · Surface temperature

1 Introduction

The fluid temperature trace in turbulent heat transfer over a flat surface shows the characteristics of periodic activities comprised of alternating large fluctuations and periods of quiescence (Townsend 1959; Howard 1966). Sparrow et al. (1970) observed that these periodic activities are due to mushroom-like structures of ascending warm fluid caused by instability due to buoyant forcing (Howard 1966). Similar structures consisting of ascending warm fluid are also observed in the surface layer of a convective boundary layer (CBL) and known as surface-layer plumes. These plumes have diameters on the order of the surface-layer height, advection velocities close to the average wind speed over their depth, are tilted by about 45° due to wind shear, and are responsible for the majority of total momentum and heat transport (Kaimal and Businger 1970; Wyngaard et al. 1971; Kaimal et al. 1976; Wilczak and Tillman 1980; Wilczak and Businger 1983; Renno et al. 2004). As these plumes ascend through the CBL, they combine with each other to create thermals in the mixed layer.

Conditional averaging of surface-layer plumes by Schols (1984) and Schols et al. (1985) revealed that the resulting air-temperature trace shows ramp-like patterns. Gao et al. (1989), Paw et al. (1992), Braaten et al. (1993) and Raupach et al. (1996) studied these temperature ramp patterns over different canopies and modelled the transport process using the surface renewal method. The surface renewal method conceptualizes the heat exchange process to occur based on coherent structures: a cold air parcel descends to the ground during the sweep event, while it remains close to the ground it is heated, and when it achieves sufficient buoyancy the warm air parcel ascends during the ejection event. The surface renewal method has been successfully employed to estimate sensible and latent heat fluxes over different canopies by Paw et al. (1995), Snyder et al. (1996); Spano et al. (1997, 2000); Castellvi et al. (2002); Castellvi (2004) and Casstellvi and Snyder (2009).

The effect of coherent structures on the surface temperature was first observed by Derksen (1974) and Schols et al. (1985) who found streaky patterns of surface temperature with about a 2°C heterogeneity along the wind direction using an airborne thermal infra-red (IR) camera. Hetsroni and Rozenblit (1994), Hetsroni et al. (2001), and Gurka et al. (2004) observed a similar streaky structure in surface temperature in a laboratory convective water flume experiment at different Reynolds numbers. High surface-temperature streaks corresponded to low velocity fluid streaks in the boundary layer and the distance between streaks increased with Reynolds number. Using an IR temperature sensor Paw et al. (1992), Katul et al. (1998) and Renno et al. (2004) observed surface-temperature fluctuations in the CBL with an amplitude of 0.5°C over 2.6-m high maize crops, greater than 2°C over 1-m high grass, and 2–4°C over a desert area, respectively. Using IR imagery, Ballard et al. (2004); Vogt (2008) and Christen et al. (2012) observed spatial heterogeneities in the magnitude of surface-temperature fluctuations over a grass canopy, a bare field, and in an urban environment, respectively.

Direct numerical simulation (DNS) of turbulent heat transfer coupled with heat conduction in the adjacent solid by Tiselj et al. (2001) revealed that the magnitude of surface-temperature fluctuations depends on the wall thickness and relative strength of thermal response times for the solid and fluid. Balick et al. (2003) identified similar key parameters for the coupled heat transfer process at the earth's surface. Hunt et al. (2003) observed different forms of coherent structures (plumes and puffs) by varying the surface thermal properties in their DNS of the solid-fluid coupled turbulent heat transport process. Ballard et al. (2004) hypothesized that

high frequency surface-temperature fluctuations are caused by turbulent mixing. Katul et al. (1998) and Renno et al. (2004) argued that surface-temperature fluctuations are caused by inactive eddy motion and convective mixed-layer processes. Christen and Voogt (2009, 2010) visualized the spatial surface-temperature field in a suburban street canyon and qualitatively attributed the vertical heat transport to the observed coherent structures that were shown to move along the wind direction.

Garai and Kleissl (2011) examined surface-temperature structures and heat transport processes over an artificial turf field using 1-Hz IR imagery. Although the camera field-of-view was smaller ($48 \times 15\,m^2$) than the scale of the largest surface-temperature structures, different surface-temperature characteristics were identified corresponding to different phases of the surface renewal process. The surface-temperature field showed large cold structures during sweep events, small patches of warm structures in a cold background during the transition from sweep to ejection, large warm structures during the ejection events, and small patches of cold structures in a warm background during the transition from ejection to sweep. Sequential animation of the surface temperature showed growth and merging of thermal footprints moving along the wind direction. Garai and Kleissl (2011) speculated that these atmospheric turbulence driven surface-temperature fluctuations can induce physical "noise" in different applications of remote sensing, such as the identification of land mines, illegal land-fills and the determination of evapotranspiration for irrigation management. For example, several remote sensing models (e.g. the surface energy balance algorithm for land (SEBAL) by Bastiaanssen et al. 1998a,b) estimate sensible heat flux and evapotranspiration using Monin-Obukhov similarity theory, which relies on mean differences between the surface and air temperatures. Thus, the substantial deviation of instantaneous surface-temperature measurement by remote sensing platforms from the true mean can degrade the accuracy of local evapotranspiration estimates. The main objective for the present experimental set-up was to address the main limitation of Garai and Kleissl (2011) by increasing the small field-of-view of the IR camera. Furthermore turbulence measurements were collocated at different heights that allowed further investigation of the cause and manifestation of surface-temperature structures as a function of atmospheric stability and the interaction between thermal footprints and lower surface-layer turbulence. In Sects. 2–4 we describe the experimental set-up, results, and discussion and conclusions, respectively.

2 Experiment and Data Processing

2.1 Experimental Set-Up

The experiment was conducted as a part of the boundary layer late afternoon and sunset turbulence (BLLAST; Lothon et al. 2012) field campaign at the Centre de Recherches Atmosphériques, Lannemezan, France from 14 June to 8 July 2011 (Fig. 1). Surface-temperature data at 1 Hz were captured by a FLIR A320 Thermal IR camera, which was mounted 59 m above ground level (a.g.l.) at the 60-m tower (43°07′25.15″ N, 0°21′45.33″ E) looking towards 55° N with an inclination of 2° from 16 June to 29 June 2011. The camera overlooked a 90-mm high grass field with an albedo of 0.19. Longwave radiation (8–14 μm wavelength) from the surface was measured over 240×320 pixels and converted into surface temperature (T_s) assuming an emissivity of 0.95 (Oke 1987). The accuracy of the camera is $\pm$ 0.08 K. A coordinate system transformation and interpolation was performed to transform the original image to a Cartesian coordinate system, and resulted in a camera field-of-view of $450 \times 207 m^2$ with a uniform resolution of $4.5 \times 0.65 m^2$. A 1-h daytime average of the

Fig. 1 Google Earth map of the experimental site. The locations of the 10-m sonic anemometer tower, 60-m tower, radiation tower, and release position of radiosondes are marked. 1-h averaged surface temperature as viewed from the 60-m tower at 1200–1259 UTC (1400–1459 local time) on 27 June 2011 is overlaid. The quantitative analysis considers only the area of $y < 275$ m

surface temperature from the IR camera (overlaid on a map in Fig. 1) shows road, buildings and bare soil regions to be warmer and a small pond to be cooler than the grass regions.

Four Campbell Scientific sonic anemometer-thermometers (CSAT) measured the turbulent velocity components (u, v, w) and sonic air temperature (air temperature, T_a) at 20 Hz at 2.23, 3.23, 5.27 and 8.22 m a.g.l. inside the camera field-of-view at 43°07′39.2″ N, 0°21′37.3″ E ("Sonic Tower" in Fig. 1). Hereinafter these CSATs will be referred to as the 2-, 3-, 5- and 8-m CSATs. The CSATs were pointing towards 60°N. A coordinate system rotation was conducted to ensure $|\langle w \rangle / M| < 1\,\%$ (angled brackets denote temporal averaging and M is the horizontal wind speed) and to orient the CSAT winds into the IR camera coordinate system following Wilczak et al. (2001).

Radiosondes were released at 43°07′41″ N, 0°22′01″ E ("Sounding" in Fig. 1) every 6 h until 25 June 2011 and every 3 h thereafter providing profiles of wind speed, wind direction, air temperature, humidity up to 20 km with a vertical resolution of 5 m. A radiation measurement tower at 43°07′26″ N, 0°21′50.4″ E near the 60-m tower (Fig. 1) was equipped with Kipp & Zonen CM22 and CM21 pyranometers to measure the shortwave upwelling and downwelling irradiances, and Eppley-PIR and Kipp & Zonen CG4 pyrgeometers to measure the longwave upwelling and downwelling irradiance respectively. All radiation measurements were reported as 1-min averages. All measurement platforms were GPS synchronized to coordinated universal time (UTC), which lags local time by 2 h.

2.2 Data Processing

Ogive tests (Foken et al. 2006) revealed that an averaging period of 5 min is sufficient to estimate momentum and heat fluxes from the 2- to 8-m CSATs using the eddy-covariance

method (for details see the Appendix). To minimize the effects of changing meteorological conditions on the time series of fluctuating wind speed (u, v, w), air temperature (T_a), and surface temperature (T_s) the 5-min linear trend was removed using

$$X' = X(t) - \left(\langle X\rangle_{5\min} - a_{X,5\min} t\right), \tag{1}$$

where $a_{X,5\min}(t)$ is the linear time dependence coefficient of variable X (for surface temperature, $a_{Ts,5\min}(t, x, y)$, i.e. it is computed separately for each camera pixel). Since, there were no continuously functioning finewire thermocouples or infra-red gas analyzers on the sonic tower, the kinematic sensible heat flux was estimated using

$$\frac{H}{\rho_a C_{p,a}} \approx \frac{\langle w' T_a' \rangle}{(1 + 0.06/B)}, \tag{2a}$$

where ρ_a, $C_{p,a}$ and B are the dry air density, dry air specific heat and the Bowen ratio estimated using a CSAT and a LICOR 7500A CO_2/H_2O analyzer mounted at 29.3 m a.g.l. at the 60-m tower, operated at 10 Hz, and taking an averaging period of 10 min. The 2-m CSAT data were used to estimate the mean sensible heat flux (Eq. 2a), the friction velocity (Eq. 2b), the convective velocity (Eq. 2c), the surface-layer temperature scale (Eq. 2d), the Obukhov length (Eq. 2e), and the flux Richardson number (Eq. 2f):

$$u_* = \left(\langle u'w'\rangle^2 + \langle v'w'\rangle^2\right)^{1/4}, \tag{2b}$$

$$w_* = \left(\frac{g z_i}{\langle T_a\rangle}\frac{H}{\rho_a C_{p,a}}\right)^{1/3}, \tag{2c}$$

$$T_*^{SL} = -\frac{\left(\frac{H}{\rho_a C_{p,a}}\right)}{u_*}, \tag{2d}$$

$$L = -\frac{\langle T_a\rangle u_*^3}{\kappa g\left(\frac{H}{\rho_a C_{p,a}}\right)}, \tag{2e}$$

$$Ri_f = \frac{\frac{g}{\langle T_a\rangle}\left(\frac{H}{\rho_a C_{p,a}}\right)}{u_*^2\frac{\partial\langle M\rangle}{\partial z}}, \tag{2f}$$

where κ and g are the von Kármán constant ($= 0.4$) and the acceleration due to gravity respectively. The vertical gradient of horizontal wind speed was estimated using the Businger–Dyer similarity relationships.

Footprint functions estimate the relative contribution of scalar sources from different ground locations to the measurement location of the scalar. To calculate the footprints of different CSATs, we used the scalar footprint derived from the flux footprint model of Hsieh et al. (2000). In this model, temperature is treated as a passive scalar and the 1-D flux footprint function (f) for the unstable boundary layer is

$$f(\tilde{x}, z_m) = \frac{1}{\kappa^2\tilde{x}^2} 0.28 z_u^{0.59} |L|^{1-0.59} \exp\left(\frac{-1}{\kappa^2\tilde{x}} 0.28 z_u^{0.59} |L|^{1-0.59}\right), \tag{3a}$$

where $\tilde{x}$, z_m and z_u are the streamwise distance from the measurement tower, the measurement height and a scaled measurement height defined as $z_u = z_m(\log(z_m/z_o) - 1 + z_o/z_m)$, where z_o is the aerodynamic roughness length. The flux footprint (f) is related to scalar footprint (C) by (Kormann and Meixner 2001)

$$M\frac{\partial C}{\partial \tilde{x}} = -\frac{\partial f}{\partial z}. \tag{3b}$$

The 1-D scalar footprint function (C) was then used to calculate the 2-D scalar footprint function (C_{2D}) assuming a Gaussian distribution of zero mean and standard deviation of the wind direction (σ_θ) using

$$\sigma_{\tilde{y}} = \frac{\sigma_\theta \tilde{x}}{1+\sqrt{\frac{\tilde{x}}{400\langle M\rangle}}}, \tag{3c}$$

$$C_{2D} = \frac{C}{\sqrt{2\pi}\sigma_{\tilde{y}}} e^{-\frac{\tilde{y}^2}{2\sigma_{\tilde{y}}^2}}, \tag{3d}$$

where $\tilde{y}$ is the spanwise distance. For the comparison of 20-Hz turbulence data with 1-Hz footprint averaged surface-temperature data, a box filter of size 1 s centred at the time stamp of the surface-temperature measurement was applied on the turbulence data. Net radiation R_{net} was obtained from the radiation tower measurements, but upwelling longwave irradiance measured at the radiation tower was replaced by the average IR camera measurement.

Finally, the ground heat flux G was modelled numerically by solving the transient 3-D heat conduction equation

$$\frac{\partial T_g}{\partial t} = \alpha_g \left(\frac{\partial^2 T_g}{\partial x^2} + \frac{\partial^2 T_g}{\partial y^2} + \frac{\partial^2 T_g}{\partial z^2}\right), \tag{4a}$$

where α_g and T_g are the thermal diffusivity and the temperature of the soil respectively. The conduction equation was discretized horizontally using a spectral method with periodic boundary conditions; vertically a second-order finite difference scheme was used; the Euler implicit scheme was applied for time integration. The numerical solution of Eq. 4a was validated against the analytical solutions of constant and sinusoidally varying surface temperature (not shown). To simulate soil temperatures, homogeneous clay soil with 40 % volumetric water content was assumed yielding thermal diffusivity α_g and conductivity k_g of 0.4 mm^2s^{-1} and 0.8 $\text{W m}^{-1}\text{ K}^{-1}$ respectively (Campbell and Norman 1998). The IR temperature (T_s) was used at the top-surface boundary ($z = 0$), an adiabatic boundary condition $\left(\frac{\partial T_g}{\partial z} = 0\right)$ was used at the bottom boundary ($z = -5.5$ m) and the temperature in the domain was initiated by

$$T_g(x, y, z, t = 0) = T_\infty + \frac{\langle G\rangle}{k_g}\left\{2\left(\frac{\alpha_g \tau}{\pi}\right)^{1/2}\exp\left(-\frac{z^2}{4\alpha_g \tau}\right) + \frac{z}{2}\text{erfc}\left(-\frac{z}{2\sqrt{\alpha_g \tau}}\right)\right\}, \tag{4b}$$

where $\langle G\rangle$, τ, T_∞ and erfc are the mean ground heat flux obtained from the surface energy balance (Eq. 4c), a dummy time variable to minimize unrealistic initialization effects (Eq. 4d, Carslaw and Jaeger 1959), the soil temperature as $z \to -\infty$ (= 288 K, which is the annual average air temperature), and the complimentary error function respectively. Thus,

$$\langle G\rangle = \left\langle R_{\text{net}} - \left(1+\frac{1}{B}\right)H\right\rangle, \tag{4c}$$

$$\tau = \left[\frac{k_g\left(\langle T_s\rangle - T_\infty\right)}{2\langle G\rangle}\right]^2 \frac{\pi}{\alpha_g}. \tag{4d}$$

As the temperature gradient is largest near the surface, the vertical grid resolution was set to 1.5 mm; below $z = -0.05$ m the vertical grid was stretched uniformly to 0.1-m resolution. The simulation was spun up for 100 timesteps to limit the influence of the initial conditions. The ground heat flux G was then computed from T_g as

$$G = \left[\frac{\Delta z}{2\Delta t}\int_{\Delta t}\rho_g C_{p_g}\frac{\partial T_g}{\partial t}dt\right] - \left[\frac{\Delta z}{2\Delta x}\int_{\Delta x}k_g\frac{\partial^2 T_g}{\partial x^2}dx + \frac{\Delta z}{2\Delta y}\int_{\Delta y}k_g\frac{\partial^2 T_g}{\partial y^2}dy\right] + \left[k_g\frac{T_s - T_{g,-\Delta z}}{\Delta z}\right], \tag{4e}$$

where ρ_g, C_{pg}, Δx, Δy, Δz are density, specific heat of the soil, and grid size in the horizontal (x, y) and vertical (z) directions respectively. In Eq. 4e the first, second and third bracketed terms represent temporal storage, horizontal heat diffusion and vertical heat diffusion respectively.

3 Results

Since the surface-temperature fluctuations only exceed the noise level of the camera during unstable conditions (Garai and Kleissl 2011), only daytime data were considered for detailed analysis. Building ($y > 275$ m) and road (a straight line from $x = 65$ m at $y = 0$ to $x = 30$ m at $y = 300$ m) pixels (Fig. 1) in the IR images were omitted from the analysis, to minimize the effects of surface heterogeneity.

3.1 Meteorological Conditions

Figure 2 presents 30-min averaged meteorological conditions for the intensive observational periods consisting of the clear days during 16–27 June, 2011. Potential temperature from radiosonde data are shown in the inset of the figures. Clear days are expected to produce both stationary time periods and the most unstable stability conditions; R_{net} reaches 700 W m^{-2} at midday for all clear days. There were some early morning and late afternoon cloud periods on 24 and 26 June, respectively, and rain (about 2–2.5 mm) occurred on 18 and 22–23 June as cold fronts from the Atlantic Ocean crossed the site. Air temperature fell to 15–20°C just after the rain and increased on successive clear days. Surface temperature followed a similar trend as air temperature. Potential-temperature (Θ) profiles from radiosondes show that the inversion height (z_i) did not exhibit a strong diurnal cycle except on 20, 26 and 27 June. The height z_i was about 1 km for 19 and 24 June and 600 m for 25 June; it increased from 750 m to 1 km on 20 June, increased from 500 m to 1 km and then fell to 750 m on 26 June, and increased from 750 m to 1 km and then fell to 450 m on 27 June for the 1050, 1350, and 1650 UTC soundings, respectively. The near-surface ($z < 8$ m) wind speed was about 2.5 m s^{-1} for 19, 20 and 24 June and about 3 m s^{-1} for 25–27 June. Mixed-layer wind speed (the mean of radiosonde data from $z/z_i = 0.1$ to 0.8) was close to the 8-m wind speed for all days except 25 and 26 June, when the mixed-layer wind speed was at least 25 % larger. Wind direction was northerly for 19 and 24 June, easterly for 25 and 26 June and north-easterly for 20 and 27 June. Easterly to north-easterly flow is typical for the mountain-plain circulation in the area.

30-min periods were chosen for further investigation based on the following stationarity criteria applied to the 2-m CSAT data: constant Obukhov length, constant wind speed (stan-

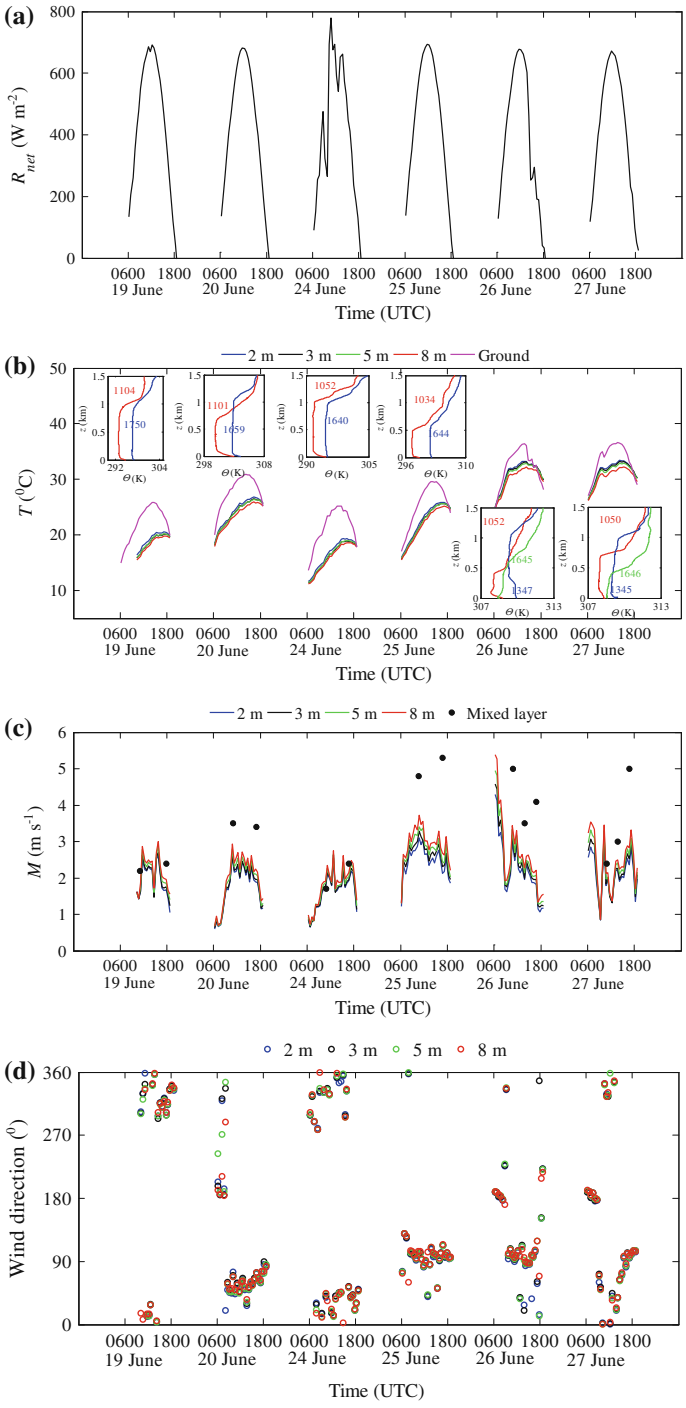

Fig. 2 30-min averages of **a** net radiation, **b** temperatures, **c** wind speed and **d** wind direction. Radiosonde potential temperature profiles are shown in the *inset* of (**b**), where the release time (HHMM UTC) is shown in colour

Table 1 Scales, stability and turbulence parameters sorted by L and Ri_f during periods classified as stationary (see text for criteria used). Inversion heights z_i were estimated visually from the radio soundings as inflection point in the potential-temperature profiles (increase in potential temperature exceeds 1 K over 100 m height)

Time (UTC)	L(m)	Ri_f	u_* (m s^{-1})	w_* (m s^{-1})	$\frac{H}{\rho_a C_{p,a}}$ (K m s^{-1})	z_i (km)
0930–1000, 27 June	−5.5	−0.66	0.15	0.95	0.045	0.6
0830–0900, 26 June	−6.7	−0.52	0.15	0.71	0.028	0.4
1100–1130, 20 June	−7.3	−0.47	0.22	1.38	0.113	0.7
1100–1130, 27 June	−8.5	−0.39	0.19	1.15	0.058	0.8
1030–1100, 27 June	−8.5	−0.39	0.18	1.06	0.053	0.7
1530–1600, 20 June	−8.8	−0.37	0.19	1.31	0.062	1.1
0935–1005, 26 June	−9.4	−0.35	0.17	0.82	0.043	0.4
0825–0855, 27 June	−10.4	−0.31	0.15	0.76	0.027	0.5
1200–1230, 25 June	−11.7	−0.27	0.26	1.23	0.112	0.5
1030–1100, 25 June	−12.5	−0.25	0.27	1.23	0.112	0.5
0900–0930, 25 June	−14.3	−0.21	0.27	1.18	0.098	0.5
1000–1030, 25 June	−14.7	−0.20	0.28	1.22	0.109	0.5
0830–0900, 25 June	−15.6	−0.19	0.26	1.10	0.079	0.5
1000–1030, 26 June	−19.5	−0.15	0.22	0.81	0.042	0.4
1115–1145, 26 June	−19.5	−0.15	0.24	1.00	0.053	0.6
1530–1600, 25 June	−19.6	−0.15	0.23	0.93	0.049	0.5
1000–1030, 27 June	−22.3	−0.13	0.26	1.10	0.059	0.7
1130–1200, 26 June	−22.8	−0.12	0.25	0.98	0.049	0.6
1130–1200, 25 June	−23.6	−0.12	0.33	1.25	0.117	0.5
1700–1730, 20 June	−36.5	−0.07	0.21	0.88	0.019	1.1
1025–1055, 26 June	−37.2	−0.07	0.29	0.87	0.051	0.4

dard deviation of the six consecutive 5-min means is less than 10 % of the 30-min mean) and constant wind direction (standard deviation of the six consecutive 5-min wind direction is less than 20°). Data from the days after the rain (19 and 24 June) were excluded, as the IR surface temperature was affected by local pooling of water. Stationary periods are characterized in Table 1 in order of increasing stability. The data from the 2-m CSAT, indicate that $Ri_f = 1.69\zeta$ with 99.7 % coefficient of determination, where $\zeta = z/L$, with $z = 2.23$ m. For the remainder of the paper, we have chosen ζ to parametrize the stability.

3.2 Spatial and Temporal Evolution of Surface and Air Temperatures and Comparison to Similarity Functions

We have chosen the time periods with $L = -10.2$ and -19.5 m to illustrate the stability dependence of surface temperature and air turbulence data, as they are representative of more unstable and less unstable conditions in our dataset with different wind directions (177° for $L = -10.2$ m and 91° for $L = -19.5$ m). Structures in the spatial surface-temperature fluctuation field are aligned with the wind direction (Fig. 3) demonstrating that the observed surface-temperature structures are not an artefact of surface heterogeneity or topography (also since temporal averages have been removed as in Eq. 1). With time these surface-temperature

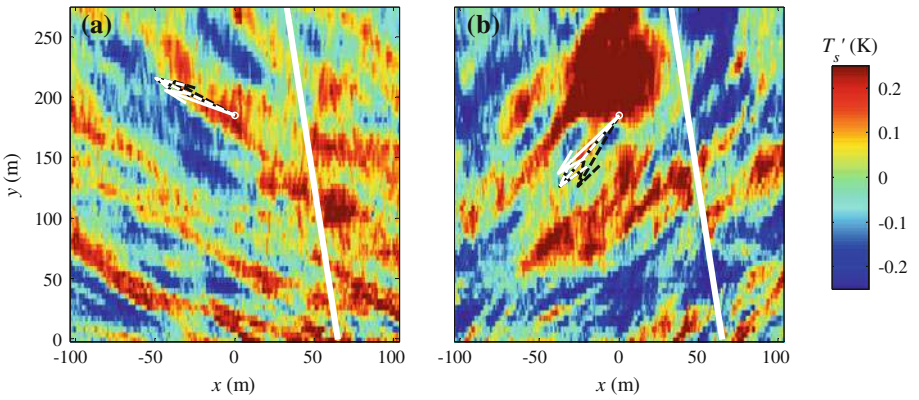

Fig. 3 Snapshots of surface-temperature fluctuations for $L = \mathbf{a} -10.2$ m at 27 June 0838 UTC, and $\mathbf{b} -19.5$ m at 26 June 1124 UTC. *Arrow lines* represent 1-s averaged wind vectors (scaled to the distance covered in 25 s) at 8 m (*black solid*), 5 m (*black dashed*), 3 m (*white solid*) and 2 m (*white dashed*) a.g.l. at the measurement location (*white circle*) respectively. The *thick white line* represents data excluded due to the road

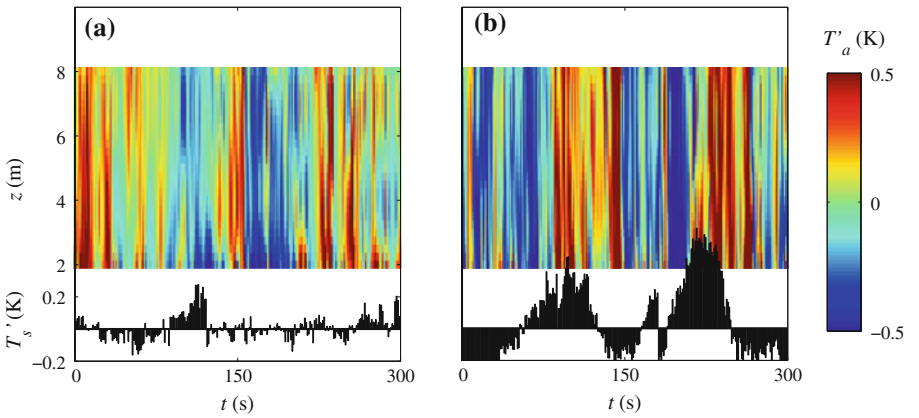

Fig. 4 Time series of air temperature (*colour bar*) and footprint-averaged surface temperature (*bar plot*) for $L = \mathbf{a} -10.2$ m at 27 June 0833–0838 UTC, and $\mathbf{b} -19.5$ m at 26 June 1122–1127 UTC. Air temperatures were vertically interpolated using spline interpolation. The footprint is the area with greater than 10 % of the maximum value of the scalar footprint function of the 2-m CSAT

structures grow, merge with each other, and move along with the airflow (see supplementary material for animations).

The temporal evolution of surface-temperature and air-temperature fluctuations at different heights are then compared in Fig. 4. The surface temperature is the average across the scalar footprint (Eqs. 3a–3d) of the 2-m CSAT with a cut-off of 10 % of the maximum value of the scalar footprint function. Fig. 4 shows that air temperature and surface temperature are highly cross-correlated and air temperature lags surface temperature since the footprint is upstream: when the surface is cold the air cools and when the surface is warm the air warms. Also, the air temperature at a lower altitude shows more small-scale fluctuations compared to the surface temperature. This is due to the fact that the surface temperature is spatially averaged across the footprint, and not as affected by the small-scale events as is air temperature, since the former has larger thermal intertia compared to the latter. Comparing Fig. 4a, b reveals

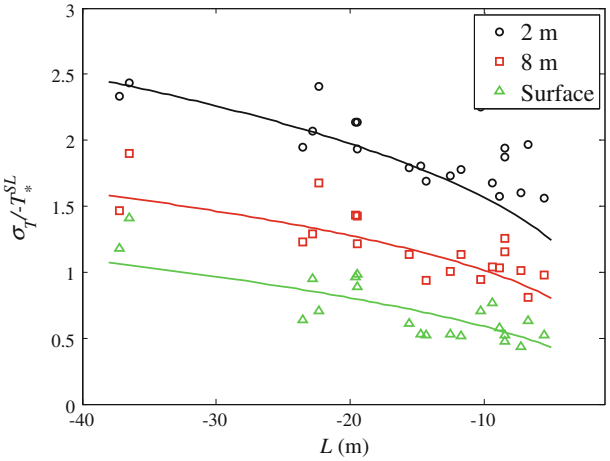

Fig. 5 Normalized standard deviations of surface temperature and air temperature as a function of L. The markers are measurements for the periods in Table 1, the *black* and *red solid lines* are fitted according to the surface-layer similarity theory $\sigma_{Ta}/T_*^{SL} = -0.95\,(-z/L)^{-1/3}$ and the *green line* is fitted to the surface-temperature standard deviation: $\sigma_{Ts}/T_*^{SL} = -0.36\,(-\zeta)^{-0.39}$

that both surface temperature and air temperature show more small-scale fluctuations as the boundary layer becomes more unstable. Similar results are obtained for all other stationary conditions.

Figure 5 shows temperature standard deviations normalized by the surface-layer temperature scale, T_*^{SL}, for all stationary periods. Normalized σ_{Ta} for 2 m and 8 m a.g.l. decrease with increasing height and stability closely following the surface-layer similarity theory, $\sigma_{Ta}/T_*^{SL} = -0.95\,(-z/L)^{-1/3}$ (Wyngaard et al. 1971). $\sigma_{Ts} < \sigma_{Ta}$ at 8 m a.g.l. and satisfies $\sigma_{Ts}/T_*^{SL} = -0.36\,(-\zeta)^{-0.39}$.

DNS of the solid-fluid coupled turbulent heat transfer by Tiselj et al. (2001) showed that σ_{Ts} depends on the solid thickness and the thermal properties of solid and fluid as in the thermal activity ratio, $TAR = \frac{k_f}{k_s}\sqrt{\frac{\alpha_s}{\alpha_f}}$, where k and α are the thermal conductivity and thermal diffusivity of the fluid (subscript "f") and the solid (subscript "s"). They found that a fluid-solid combination with low TAR does not allow imprints of fluid-temperature fluctuations on the solid surface. Balick et al. (2003) also derived a similar parameter for a coupled land-atmosphere heat transfer model. For our measurement site, one can assume the fluid-solid coupled heat transport to occur between air and homogeneous clay soil, or between air and grass leaves or a combination of both. Assuming $k_f = 0.025\,\mathrm{W\,m^{-1}\,K^{-1}}$ and $\alpha_f = 20\,\mathrm{mm^2\,s^{-1}}$, for homogeneous clay soil with 40 % volumetric water content $TAR = 0.0044$ and for grass leaves with 1000 leaves $\mathrm{m^{-2}}$ and a weight of 10^{-3} kg per leaf (i.e. $k_s = 0.38\,\mathrm{W\,m^{-1}K^{-1}}$ and $\alpha_s = 19.62\,\mathrm{mm^2\,s^{-1}}$, Jayalakshmy and Philip (2010)) $TAR = 0.07$. Under these conditions according to Tiselj et al. (2001) $\sigma_{Ts} < 1\,\%$ for soil and about 10 % for grass of its iso-flux counterpart, which corresponds to $TAR \to \infty$. Thus the air-grass leaf coupled heat transport mechanism better fits our data, as Tiselj et al. (2001) and Hunt et al. (2003) reported non-dimensional surface-temperature standard deviation of 2 when temperature is modelled as passive scalar (normalized by $\frac{H}{\rho_a C_{p,a} u_*}$) and about 3 when wind shear is absent (normalized by $\frac{H}{\rho_a C_{p,a} w_*}$) for their corresponding DNS results, respectively. However, DNS results may not apply to the field measurements, as in the DNS

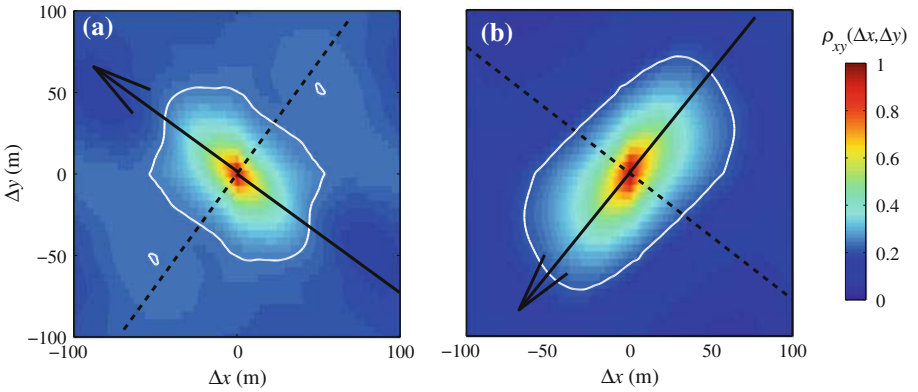

Fig. 6 Mean spatial correlation of surface temperature for **a** $L = -10.2$ m, and **b** $L = -19.5$ m (in the camera coordinate system). The *solid* and *broken black lines* indicate averaged streamwise and spanwise directions over 2, 3, 5 and 8 m a.g.l., respectively. The *white contour line* indicates a correlation of 0.25

the Reynolds number was low, a different magnitude of stability was used, and the transport of water vapour was neglected.

3.3 Spatial Scale of Surface-Temperature Structures

The spatial scale of surface-temperature structures (as seen in Fig. 3) can be investigated by considering the spatial correlation for each image using

$$\rho_{xy}\left(\Delta x, \Delta y, t\right) = \frac{\overline{T_s'\left(x, y, t\right) T_s'\left(x + \Delta x, y + \Delta y, t\right)}}{\sigma_{Ts}^2} \tag{5}$$

where the overbar indicates a spatial average. Figure 6 shows the temporal average of the spatial correlation of the surface-temperature structures $\left(\langle \rho_{xy}\left(\Delta x, \Delta y, t\right)\rangle\right)$, for (a) $L = -10.2$ m, and (b) $L = -19.5$ m. The surface-temperature correlation structures are shaped as ellipsoids with the major axis aligned with the streamwise direction.

The spatial properties of coherent structures in a boundary-layer flow depend on shear and buoyancy. For a shear-dominated boundary layer, the structures become elongated in the direction of flow and streaky, whereas for a buoyancy-dominated boundary layer, they become more circular. We consider u_* as a measure of shear and ζ as a relative measure of buoyancy to study their effect on the surface-temperature structures. Figure 7 shows, (i) the streamwise correlation length (l_{stream}), and (ii) the aspect ratio ($AR = l_{\text{stream}}/l_{\text{span}}$, where l_{span} is the spanwise correlation length) against ζ and u_* for all stationary periods. The correlation length is defined as twice the distance from the centre where the correlation becomes 0.25 in the streamwise and spanwise directions (Fig. 6). Though the quantitative values of the streamwise and spanwise lengths will depend on the chosen cut-off correlation, the qualitative behaviour of the streamwise and spanwise lengths with stability and friction velocity are independent of the chosen correlation cut-off value. The spatial scales of surface-temperature structures will also depend on the averaging period, as the camera field-of-view could not capture the largest possible structure in CBL. A 30-min averaging period resulted in structures 20–40 % larger than those computed using a 5-min averaging period. With increasing stability the structures become streakier. Thus *AR* is close to unity for the more unstable cases and larger than unity for the less unstable cases. Hommema and Adrian (2003) and Li and Bou-Zeid (2011)) also

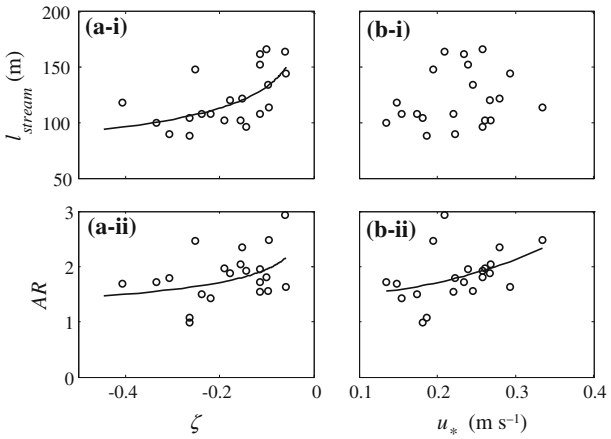

Fig. 7 **i** Streamwise correlation length l_{stream}, and **ii** aspect ratio AR of the mean surface-temperature structure with **a** ζ and **b** u_*. *Markers* represent the measurements and *solid lines* represent fits: $l_{\text{stream}} = 78.03\,(-\zeta)^{-0.23}$, $AR = 1.26\,(-\zeta)^{-0.19}$, $AR = 11.43u_*^2 - 1.5u_* + 1.55$ with 48.6, 28.0 and 27.7 % coefficient of determination respectively. No trend was observed and no line was fitted for **b-i**

reported that, as the boundary layer becomes more unstable, the dominant coherent structures in the surface layer change from long streaky structures due to hairpin packets to surface-layer plumes. l_{stream} does not show any recognizable trend against u_*, but AR increases from 1.5 for small u_* to > 2 for larger u_*. Wilczak and Tillman (1980) reported similar streamwise sizes of coherent structures based on the time traces of air temperature at 4 m a.g.l..

3.4 Surface-Temperature and Air-Temperature Correlation

Since the footprint-averaged surface temperature is correlated with air temperature (Fig. 4), spatial maps of cross-correlation between surface temperature and air temperature were generated using

$$\rho_{Ts,Ta}\,(x,\,y,\,\Delta t) = \frac{\langle T_s'\,(x,\,y,\,t)\;T_a'\,(x_o,\,y_o,\,t+\Delta t)\rangle}{\sigma_{Ts}\sigma_{Ta}}, \tag{6}$$

where x_o and y_o are the coordinates of the sonic tower and the two vectors are lagged by up to $\Delta t = 60$ s. To reduce noise in the cross-correlation maps, an ensemble average of three cross-correlation maps for each 10-min interval in a 30 min-stationary period was computed. Spatial maps of maximum cross-correlations between surface temperature and air temperature at, (i) 2 m, and (ii) 8 m a.g.l. are shown in Fig. 8. The region of maximum cross-correlation between surface temperature and air temperature is elongated in the wind direction. The upwind correlation region and the scalar footprint function show significant overlap (however, note the footprint obviously only extends upwind while the correlation region extends upwind and downwind). Specifically, the cross-wind spread of the maximum correlation region is similar to that of the footprint function (Eqs. 3c-d). The maximum correlation coefficient, size of the correlation region, and the footprint increase when the 8-m air temperature is correlated with the surface temperature. Similar trends are also observed for the other stationary periods.

Along the wind direction cross-correlations between the air temperature at 8 m a.g.l. and the lagged surface temperature (Fig. 8ii) are then plotted in Fig. 9i. Here, positive r indicates

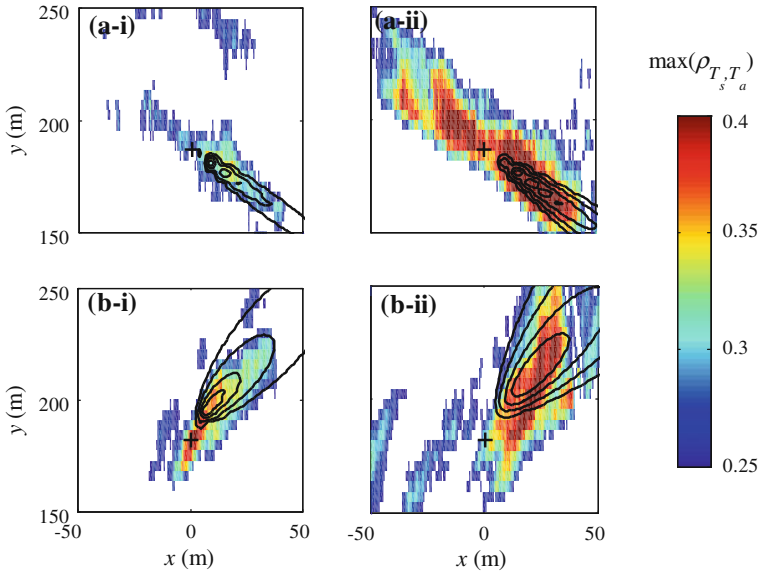

Fig. 8 30-min maximum cross-correlation between surface temperature and air temperature at, **i** 2 m and **ii** 8 m with scalar footprint model (Eq. 3a–3d, *black contours*) for **a** $L = -10.2$ m, and **b** $L = -9.5$ m. *White pixels* represent surface-temperature and air-temperature correlation < 0.25 or unreasonable lags (absolute lag > 60 s). The *black contour lines* represent 10, 25, 50 and 75 % of the maximum of scalar footprint function. The *black* '+' sign marks the location of the sonic tower ($x_o = 0.4$ m and $y_o = 185$ m)

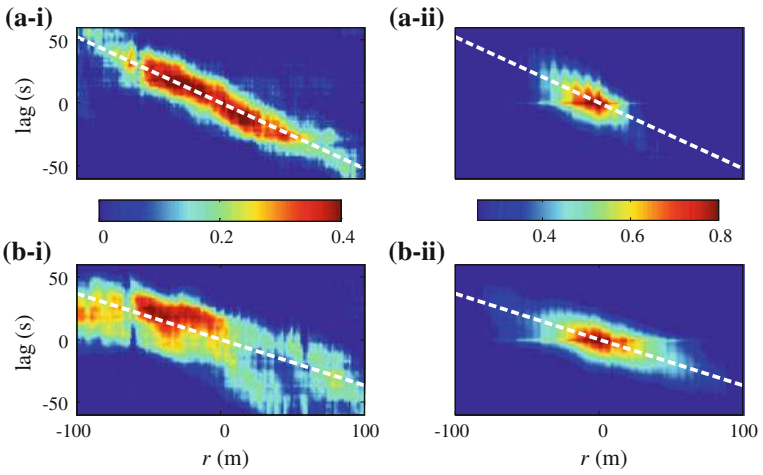

Fig. 9 *Left panels* Cross-correlation between air temperature at 8 m with surface temperature along the 8-m wind direction at different lags. *Right panels* Cross-correlation amongst surface temperature along the 8-m wind direction at different lags. **a** $L = -10.2$ m, and **b** $L = -19.5$ m. The *white dashed line* represents the slope of the cross-correlation area

the downwind direction and positive lags indicate that the surface is preceding the air and vice versa. The largest cross-correlations for the upwind (downwind) correlation region occur at a positive (negative) lag (shown in Fig. 9i). Thus the upwind surface temperature is affecting

the air temperature at the measurement location and the air temperature at the measurement location is affecting the downwind surface temperature, consistent with Garai and Kleissl (2011). Cross-correlations between surface temperatures along the wind direction are shown in Fig. 9ii as calculated using

$$\rho_{Ts,Ts}\,(r,\,\Delta t : x_*,\,y_*) = \frac{\langle T_s'\,(x_* + r\cos\theta,\,y_* + r\sin\theta,\,t + \Delta t)\,T_s'\,(x_*,\,y_*,\,t)\rangle}{\sigma_{Ts}^2}, \qquad (7)$$

where x_*, y_* and θ are arbitrary coordinates in the image and wind direction. To reduce the noise of the cross-correlation between surface temperatures, ensemble averages from 15 different (x_*, y_*) positions were computed. Note the distinction between these cross-correlations versus the spatial correlations $\rho_{xy}\,(\Delta x, \Delta y, t)$ described in Sect. 3.3; the former 'tracks' surface-temperature structures by co-varying space (r) and time (Δt), while the latter correlates structures that are not time shifted across space. Therefore, $\rho_{xy}\,(\Delta x, \Delta y, t)$ represents the typical spatial extent of surface-temperature structures at a given time and $\rho_{Ts,Ts}\,(r, \Delta t : x_*, y_*)$ represents the spatio-temporal region of influence of a given structure. If a structure remained unchanged as it moves across the image, $\rho_{Ts,Ts}\,(r, \Delta t : x_*, y_*)$ would be large.

For the correlations between surface temperatures, a positive lag indicates that the upwind surface temperature is preceded by downwind surface temperature. The cross-correlations between the surface temperatures in Fig. 9ii are larger compared to the cross-correlations between air temperature and surface temperature in Fig. 9i as the latter is calculated between two different variables and heights. Since the spatial extent of the high correlation region between the air temperature and surface temperature depends on the air-temperature measurement height, it is not useful to compare quantitatively the spatial extents of the high correlation regions for air temperature and surface temperature with that for the surface temperatures at a given stability. Qualitatively, as the stability of the boundary layer increases, the spatial extent of the high correlation region between air temperature and surface temperature, and between surface temperatures increases. A less unstable boundary layer will contain longer turbulence structures, which is manifested in the larger footprints in Fig. 9i. The cross-correlations between air temperature and surface temperature; and between surface temperatures, allow tracking the advection speed of the structures responsible for land-atmosphere exchange.

3.5 Advection Speed of the Surface-Temperature Structures

The cross-correlation surfaces between air temperature and surface temperature, and between surface temperatures, in Fig. 9 show similar slopes for a given stationary period, which is further evidence for the advective nature of the surface-temperature coherent structures. The slope of the cross-correlation indicates the advection speed u_s of the surface-temperature structures (or rather the turbulent coherent structures that leave an imprint on the surface) along the wind direction. The estimated advection speeds for all stationary periods are plotted in Fig. 10. The scatter in the plot is mostly due to the uncertainty in estimating the slope; for some wind directions the high correlation region is discontinuous (as seen in Figs. 8b–ii, 9b–i) due to surface heterogeneity. The advection speeds are similar to the wind speed at 8 m a.g.l. with a decreasing trend in less unstable conditions.

Wilczak and Tillman (1980) also reported that the speeds of surface-layer plumes are greater than the wind speed at 4 m a.g.l. with a small decreasing trend with stability. As the surface layer becomes less unstable, the strength of buoyant production decreases compared to shear production, resulting in less turbulent mixing. This causes a larger vertical gradient of horizontal wind speed in the upper part of the surface layer and also a smaller effective

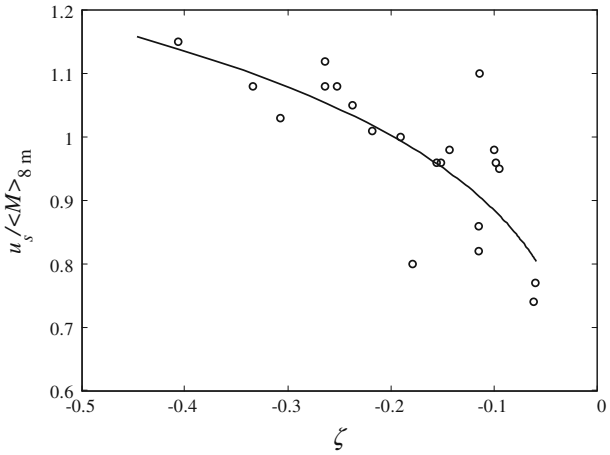

Fig. 10 Advection velocity of the surface-temperature structures (determined from Fig. 9) versus the 8-m wind speed as a function of ζ. *Markers* represent the measurements and the *solid line* represents the fitted equation $u_s/\langle M\rangle_{8\mathrm{m}} = 1.34\,(-\zeta)^{0.18}$ with 57.1 % coefficient of determination

plume height. The advection speed, i.e. the mean wind speed over the height of the surface-layer plume, should be identical to u_s of the surface-temperature coherent structures. Thus, with increase in the stability of the boundary layer u_s decreases compared to the wind speed at a sufficiently large altitude (e.g. 8 m a.g.l. in this case). Also as seen in Fig. 2c, except for 25 June the mixed-layer wind speed is similar to the wind speed at 8 m a.g.l. Consequently, one can conclude that u_s is similar to the mixed-layer wind speed. This is consistent with Katul et al. (1998) and Renno et al. (2004) who, in the absence of thermal imagery, resorted to more elaborate spectral analysis to suggest that surface-temperature structures are induced by mixed-layer turbulence.

3.6 Conditional Averaging of Ejection Events

To study the coupling between surface temperature and near-surface coherent structures in more detail, conditional averaging was employed. Events are classified as strong ejection events if $w'T'_{a\,8m} > 0.5\langle w'T'_a\rangle_{8m}$, w' is positive, and the minimum duration of the event is 3 s. Also, if two consecutive events are separated by less than 5 s, they are merged into a single event. The events are then verified by visual inspection of the time series to avoid false identification. These criteria result in 20–30 ejection events per stationary period with time scales ranging from 3 to 45 s. Since the duration of each ejection event is different, time was normalized by the individual ejection time scale such that $t = 0$ and 1 indicates the start and end of the ejection event at 8 m a.g.l. respectively.

The events cover around 20–25 % of each 30-min stationary period, but are responsible for 60–70 % of the sensible heat flux. The ejection event is initiated by surface heating (Fig. 11i). Since net radiation is nearly constant during the short duration of the event, the increase in ground heat flux associated with surface heating has to be balanced by decreases in the convective fluxes. Thus before the ejection event, $w'T'_a$ is small. During the ejection event (Fig. 11i) the warm air rises due to buoyancy, forming a surface-layer plume. The majority of the vertical heat flux occurs at the end of the ejection event (Fig. 11ii) and buoyant production increases compared to shear production (Fig. 11iii). After the ejection event, a downward

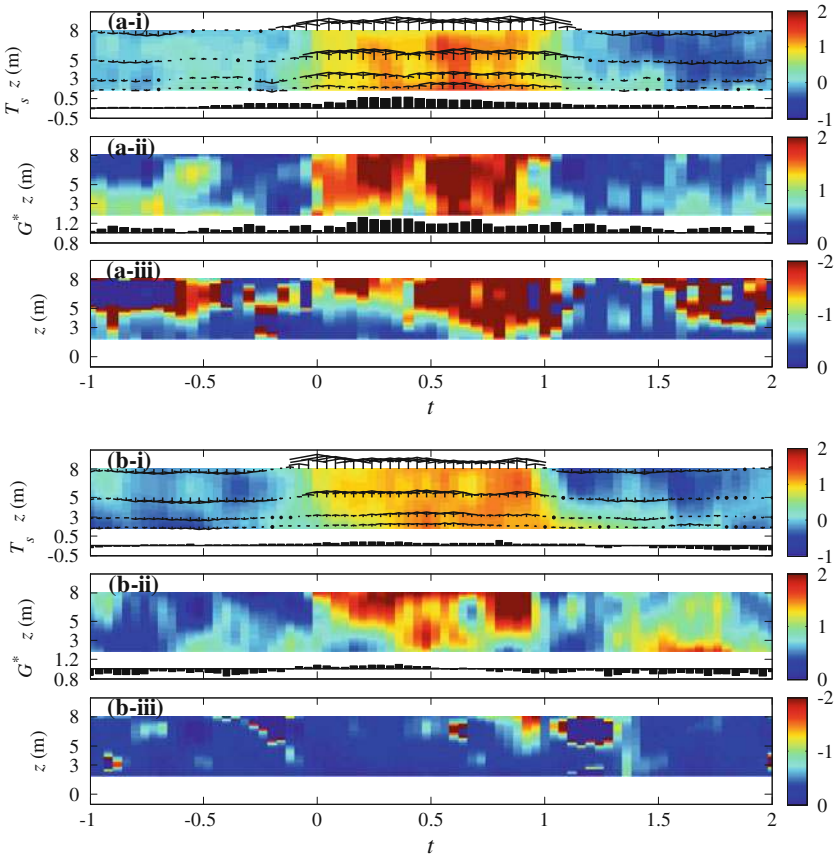

Fig. 11 Conditional average of ejection events occurring for **a** $L = -10.2$ m, and **b** $L = -19.5$ m. (**i**) air temperature (*colour*), and surface temperature (*bars*), both normalized by $-T_*^{SL}$. Vertical velocity vectors are overlayed (the largest vectors correspond to 0.4 m s^{-1}). To convert surface temperature to a time series, Taylor's frozen turbulence hypothesis was applied using the advection speed of surface-temperature structures (Fig. 9). (**ii**) $w'T_a'$ normalized by $\langle w'T_a' \rangle_{2m}$ (*colour*) and modelled ground heat flux normalized by mean ground heat flux (G^*, *bars*). (**iii**) Ri_f. The time axes are normalized such that $t = 0$ and 1 correspond to the start and the end of the ejection event at 8 m a.g.l., respectively. Note that the surface temperature is not deduced from the footprint of the air temperature, but rather the temperature directly below the air-temperature measurements

flow of cold air occurs as a sweep event. The large convective heat flux during the ejection leads to cooling of the surface and as a result the ground heat flux decreases until the end of the sweep event. Also, note that though air temperature shows a ramp-like pattern (air temperature remains almost constant during the sweep, gradually increases during the sweep to ejection transition, attains maximum at the ejection and falls sharply during the ejection to sweep transition), the change in surface temperature is smoother (gradual increase and decrease during sweep to ejection and to sweep events). This might be attributed to the higher thermal inertia of the surface compared to the air, so that small-scale variations average out over the surface.

Though air temperature and surface temperature follow similar trends, there is a time lag; the surface temperature reaches its maximum before the air temperature and its minimum

after the air temperature consistent with Garai and Kleissl (2011). Also, from Figs. 11i, it is evident that the plumes are slightly tilted due to wind shear. Since the shear production decreases more rapidly with height than buoyant production, the magnitude of Ri_f increases with height (Fig. 11iii). Also, the magnitude of Ri_f during the ejection event decreases with increasing stability of the boundary layer. Similar results are obtained for the other stationary periods.

Although the magnitude of G depends on the thermal properties of the ground, the ground heat flux normalized by the mean, $G^* = G/\langle G \rangle$, is independent of ground thermal properties since the ground conduction model is linear. Fig. 11ii shows that the ejection and sweep events cause variations of up to $0.3G$.

4 Discussion and Conclusion

Coupled land-atmosphere heat transfer was examined using lower surface-layer eddy-covariance measurements and IR surface-temperature imagery for a range of unstable conditions in the CBL. The sequential IR images of surface temperature show that temperature patterns in the surface grow, combine with each other and move along with the wind. These surface-temperature patterns can be interpreted to be the imprints of turbulent coherent structures on the surface in a CBL (Derksen 1974; Schols et al. 1985; Paw U et al. 1992; Katul et al. 1998; Balick et al. 2003; Ballard et al. 2004; Renno et al. 2004; Vogt 2008; Christen and Voogt 2009, 2010; Christen et al. 2012; Garai and Kleissl 2011). When the surface-temperature standard deviation is compared with the air-temperature standard deviation, this follows a similar trend with respect to stability and the former is smaller in magnitude than the latter at 8 m a.g.l. The normalized σ_{Ts} gives a similar power-law exponent (0.39) compared to surface-layer similarity theory (Wyngaard et al. 1971); the coefficient of proportionality differs significantly (for our data, 0.36), but it should depend on the surface thermal property (Tiselj et al. 2001; Balick et al. 2003). Different σ_{Ts} over different surfaces (σ_{Ts} over metallic roofs > lawns > roads > building walls) were also reported by Christen et al. (2012) for an urban measurement site.

Cross-correlating surface temperature and air temperature, the maximum correlation region is aligned with the wind direction. The cross-wind span of the correlation region increases with the standard deviation of the wind direction. The upwind correlation region corresponds well to the scalar footprint formulated from the model by Hsieh et al. (2000). The lag associated with the maximum correlation reveals that the upwind surface-temperature fluctuations affect the air-temperature fluctuations at the measurement tower and the air-temperature fluctuations at the measurement tower affect the downwind surface-temperature fluctuations. This indicates that vertically coherent structures advect cold and warm fluid downwind and these structures leave a temperature footprint on the surface. The correlation between footprint-averaged surface temperature with air temperature increases from 2 to 8 m. All these observations point to the surface-temperature fluctuations being caused by turbulent coherent structures in the atmospheric boundary layer.

The mean streamwise size of the surface-temperature structures (or rather the turbulent coherent structures that leave an imprint on the surface) decreases with ζ. The aspect ratio (AR) of the structures increases with both u_* and ζ. Wilczak and Tillman (1980) also reported similar sizes of coherent structures and their advection speed in the CBL by considering the time trace of air temperature at 4 m a.g.l.. These findings further substantiate that the surface-temperature patterns reflect common properties of turbulent coherent

structures in the boundary layer. More unstable flows cause more circular and shorter coherent structures while more neutral flows give rise to longer, streaky patterns, consistent with the observations of Hommema and Adrian (2003) and Li and Bou-Zeid (2011). Katul et al. (2011) related the change in the coherent structures with instability to the Businger–Dyer relationships.

The advection speed of the structures was of the order of the wind speed at 8 m a.g.l. and it decreased with stability. The mixed-layer wind speed was almost the same as the wind speed at 8 m a.g.l.. Similar results were reported by Christen and Voogt (2009, 2010) and Garai and Kleissl (2011). Katul et al. (1998) and Renno et al. (2004) inferred that high frequency surface-temperature fluctuations were caused by mixed-layer turbulence.

The surface-temperature coherent structures are finally interpreted in the context of the surface renewal method. While the Lagrangian concept of the surface renewal method cannot be conclusively demonstrated in the Eulerian measurement framework, the observations give rise to the following interaction between coherent structures and the surface. During the sweep event, a cold air parcel descends and the surface cools due to enhanced temperature differences and heat transfer between surface and air. The cooler surface results in a smaller ground heat flux during this time (Fig. 11i, ii; $t > 1$ or $-1 < t < -0.5$). As the air parcel remains in contact with the surface it warms gradually, reducing heat transfer between the surface and the air. The ground heat flux increases during this time. Thus, the surface starts to warm (Fig. 11i, ii; $-0.5 < t < 0$). As the air parcel warms up, it gains buoyancy (Fig. 11iii). With sufficient buoyancy (and possibly assisted by mixed-layer turbulence) the air parcel ascends in an ejection event. During the initial period of the ejection event, the ground heat flux reaches a maximum (Fig. 11i; $0 < t < 0.5$). As the ejection event continues greater heat transfer occurs between the surface and the air (Fig. 11ii; $0 < t < 0.5$). Afterwards the surface starts to cool and the ground heat flux starts to decrease (Fig. 11ii; $t > 0.5$).

In Garai and Kleissl (2011), we also analyzed surface-temperature structures during different phases of the surface renewal cycle. In this study, with the larger camera field-of-view and availability of air temperature at different heights, we have successfully visualized surface renewal events both in the surface layer and on the surface. However, due to the larger camera field-of-view in this study, a single image contains several surface renewal events at different stages (Fig. 3). Thus the size of the surface-temperature structure for each individual surface renewal event is averaged out when spatial correlation within an image is considered (Sect. 3.3). While it cannot be demonstrated in this study, we expect the temporal evolution of the structure size to be similar, as found in Garai and Kleissl (2011): during the ejection event there will be a large positive surface-temperature structure, during the sweep event there will be a large negative surface-temperature structure, at the transition from ejection to sweep there will be small patches of negative surface-temperature structures, and at the transition from sweep to ejection there will be small patches of positive surface-temperature structures. These surface-temperature structures grow, combine with each other and move along the higher altitude flow. Strong sweep events are followed by ejection events and the heat transfer mechanism repeats itself. We observed that the surface reaches maximum temperature before the air and minimum temperature after the air. The majority of heat transport occurs during the ejection event (about 60–70 % of the total sensible heat flux), which also causes ground heat-flux variations (about 30 % of the mean ground heat flux) through the surface energy budget.

These surface-temperature coherent structures with spatial scales of several hundred m and temperature variations of 0.5–1 K, depending on the boundary-layer instability, can reduce the accuracy of different remote sensing applications. The turbulence-induced

surface-temperature variations should also be accounted for in numerical models, since they produce considerable surface energy budget anomalies.

Acknowledgments We thank (i) Daniel Alexander from University of Utah, USA; Dr. Marie Lothon, Dr. Fabienne Lohou, Solene Derrien from Laboratoire d'Aérologie, Université de Toulouse, France; Dr. Arnold Moene, Dr. Oscar Hartogensis, Anneke Van de Boer from Wageningen University, Netherlands for field assistance, data sharing and discussion; (ii) Peter Cottle and Anders Nottrott from University of California, San Diego for pre-experimental laboratory assistance and discussion about the data analysis respectively; (iii) BLLAST organizers for their hospitality during the experiment; (iv) funding from a NASA New Investigator Program award for AG and JK, and from INSU-CNRS (Institut National des Sciences de l'Univers, Centre national de la Recherche Scientifique, LEFE-IDAO program), Météo-France, Observatoire Midi-Pyrénées (University of Toulouse), EUFAR (EUropean Facility for Airborne Research) and COST ES0802 (European Cooperation in the field of Scientific and Technical) for the BLLAST field experiment.

5 Appendix

The ogive function can be employed to estimate the sufficient averaging period for calculation of turbulent fluxes using the eddy-covariance method. Ogive ($og_{w.X}(f_o)$) is a cumulative integral of the cospectrum, $Co_{w,X}$, of a variable, X, with vertical velocity, w, starting with the highest frequency, f, $og_{w.X}(f_o) = \int_{\infty}^{f_0} Co_{w,X}(f)\,df$. Ideally the ogive function increases during the integration from high frequency to small frequency, until reaching a constant value. Hence the period corresponding to the frequency at which the ogive reaches the constant value is considered to be sufficient to capture the largest turbulence scales. To improve the statistical significance and minimize the effect of diurnal cycles, twenty-six 30-min segments for each clear days corresponding to 0600–1900 UTC were used. It was found that a 5-min averaging period accounts for 90 and 85% of the maximum value of ogive for 2- and 8-m CSATs respectively for the sensible heat flux (Fig. 12) and the momentum flux (not shown). Thus an averaging period of 5-min was selected.

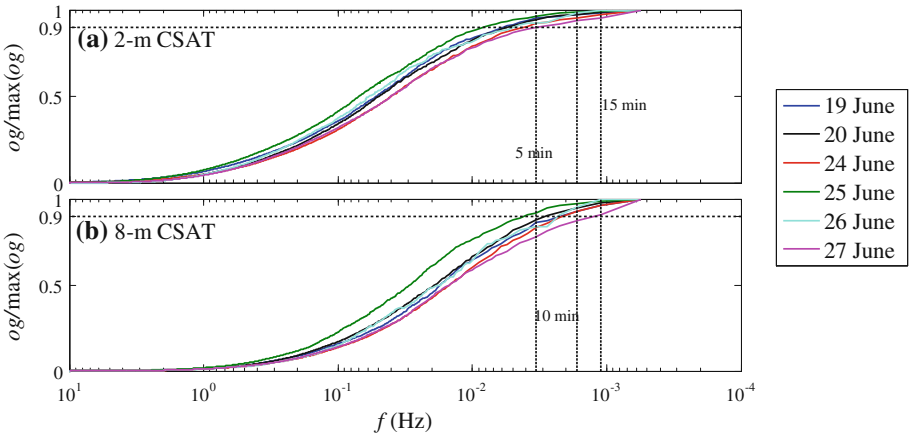

Fig. 12 The normalized ogive by its maximum value for heat-flux calculation from the 2-m and 8-m CSATs for all the clear days

References

Balick LK, Jeffery CA, Henderson B (2003) Turbulence induced spatial variation of surface temperature in high resolution thermal IR satellite imagery. Proc SPIE 4879:221–230

Ballard JR, Smith JA, Koenig GG (2004) Towards a high temporal frequency grass canopy thermal IR model for background signatures. Proc SPIE 5431:251–259

Bastiaanssen WGM, Menenti M, Feddes RA, Holstag AAM (1998a) A remote sensing surface energy balance algorithm for land (SEBAL) 1 formulation. J Hydrol 212–213:198–212

Bastiaanssen WGM, Pelgrum H, Wang J, Ma J, Moreno JF, Roerink GJ, van der Wal T (1998b) A remote sensing surface energy balance algorithm for land (SEBAL) 2 validation. J Hydrol 212–213:213–229

Braaten DA, Shaw RH, Paw UKT (1993) Boundary-layer flow structures associated with particle reentrainment. Boundary-Layer Meteorol 65:255–272

Campbell GS, Norman JM (1998) An introduction to environmental biophysics. Springer, New York, 286 pp

Carslaw HS, Jaeger JC (1959) Conduction of heat in solids. Oxford University Press, London, 510 pp

Castellvi F (2004) Combining surface renewal analysis and similarity theory: a new approach for estimating sensible heat flux. Water Resour Res 40:W05201

Castellvi F, Snyder RL (2009) Combining the dissipation method and surface renewal analysis to estimate scalar fluxes from the time traces over rangeland grass near Ione (California). Hydrol Process 23:842–857

Castellvi F, Perez PJ, Ibanez M (2002) A method based on high-frequency temperature measurements to estimate the sensible heat flu avoiding the height dependence. Water Resour Res 38(6):1084

Christen A, Voogt JA (2009) Linking atmospheric turbulence and surface temperature fluctuations in a street canyon. Paper no. A3–6. The 7th international conference on urban climate, Yokohoma

Christen A, Voogt JA (2010) Inferring turbulent exchange process in an urban street canyon from high-frequency thermography. Paper no. J3A.3. 9th symposium on the urban environment, Keystone

Christen A, Meier F, Scherer D (2012) High-frequency fluctuations of surface temperatures in an urban environment. Theor Appl Climatol 108:301–324

Derksen DS (1974) Thermal infrared pictures and the mapping of microclimate. Neth J Agric Sci 22:119–132

Foken T, Wimmer F, Mauder M, Thomas C, Liebethal C (2006) Some aspects of the energy balance closure problem. Atmos Chem Phys 6:4395–4402

Gao W, Shaw RH, Paw UKT (1989) Observation of organized structure in turbulent flow within and above a forest canopy. Boundary-Layer Meteorol 47:349–377

Garai A, Kleissl J (2011) Air and surface temperature coupling in the convective atmospheric boundary layer. J Atmos Sci 68:2945–2954

Gurka R, Liberzon A, Hestroni G (2004) Detecting coherent patterns in a flume by using PIV and IR imaging techniques. Exp Fluids 37:230–236

Hestroni G, Rozenblit R (1994) Heat transfer to a liquid-solid mixture in a flume. Int J Multiphase Flow 20:671–689

Hestroni G, Kowalewski TA, Hu B, Mosyak A (2001) Tracking of coherent thermal structures on a heated wall by means of infrared thermography. Exp Fluids 30:286–294

Hommema SE, Adrian RJ (2003) Packet structure of surface eddies in the atmospheric boundary layer. Boundary-Layer Meteorol 106:147–170

Howard LN (1966) Convection at high Rayleigh number. In: Görtler H (ed) Proceedings of the 11th international congress on applied mechanics. Springer, San Diego, pp 1109–1115

Hsieh C-I, Katul GG, Chi T (2000) An approximate analytical model for footprint estimation of scalar fluxes in thermally stratified atmospheric flows. Adv Water Resour 23:765–772

Hunt JCR, Vrieling AJ, Nieuwstadt FTM, Fernando HJS (2003) The influence of the thermal diffusivity of the lower boundary on eddy motion in convection. J Fluid Mech 491:183–205

Jayalakshmy MS, Philip J (2010) Thermophysical properties of plant leaves and their influence on the environment temperature. Int J Thermophys 31:2295–2304

Kaimal JC, Businger JA (1970) Case studies of a convective plume and a dust devil. J Appl Meteorol 9:612–620

Kaimal JC, Wyngard JC, Haugen DA, Cote OR, Izumi Y (1976) Turbulence structure in the convective boundary layer. J Atmos Sci 33:2152–2169

Katul GG, Schieldge J, Hsieh C-I, Vidakovic B (1998) Skin temperature perturbations induced by surface layer turbulence above a grass surface. Water Resour Res 34:1265–1274

Katul GG, Konings AG, Porporato A (2011) Mean velocity profile in a sheared and thermally stratified atmospheric boundary layer. Phys Rev Lett 107:268502

Kormann R, Meixner FX (2001) An analytical footprint model for non-neutral stratification. Boundary-Layer Meteorol 99:207–224

Li D, Bou-Zeid E (2011) Coherent structures and the dissimilarity of turbulent transport of momentum and scalars in the unstable atmospheric surface layer. Boundary-Layer Meteorol 140:243–262

Lothon M, Lohou F, Durand P, Couvreux Sr. F, Hartogensis OK, Legain D, Pardyjak E, Pino D, Reuder J, Vilà Guerau de Arellano J, Alexander D, Augustin P, Bazile E, Bezombes Y, Blay E, van de Boer A, Boichard JL, de Coster O, Cuxart J, Dabas A, Darbieu C, Deboudt K, Delbarre H, Derrien S, Faloona I, Flament P, Fourmentin M, Garai A, Gibert F, Gioli B, Graf A, Groebner J, Guichard F, Jonassen M, van de Kroonenberg A, Lenschow D, Martin S, Martinez D, Mastrorillo L, Moene A, Moulin E, Pietersen H, Piguet B, Pique E, Román-Cascón C, Said F, Sastre M, Seity Y, Steeneveld GJ, Toscano P, Traullé O, Tzanos D, Wacker S, Yagüe C (2012) The boundary layer late afternoon and sunset turbulence 2011 filed experiment. Paper no. 14B.1. 20th symposium on boundary layers and turbulence, Boston

Oke TR (1987) Boundary layer climates. Methuen, London, 435 pp

Paw UKT, Brunet Y, Collineau S, Shaw RH, Maitani T, Qiu J, Hipps L (1992) On coherent structures in turbulence above and within agricultural plant canopies. Agric For Meteorol 61:55–68

Paw UKT, Qiu J, Su H-B, Watanabe T, Brunet Y (1995) Surface renewal analysis: a new method to obtain scalar fluxes. Agric For Meteorol 74:119–137

Raupach MR, Finnigan JJ, Brunet Y (1996) Coherent eddies and turbulence in vegetation canopies: the mixing-layer analogy. Boundary-Layer Meteorol 78:351–382

Renno NO, Abreu VJ, Koch J, Smith PH, Hartogensis OK, De Bruin HAR, Burose D, Delory GT, Farrell WM, Watts CJ, Garatuza J, Parker M, Carswell A (2004) MATADOR 2002: a pilot experiment on convective plumes and dust devils. J Geophys Res 109:E07001

Schols JLJ (1984) The detection and measurement of turbulent structures in the atmospheric surface layer. Boundary-Layer Meteorol 29:39–58

Schols JLJ, Jansen AE, Krom JG (1985) Characteristics of turbulent structures in the unstable atmospheric surface layer. Boundary-Layer Meteorol 33:173–196

Snyder RL, Spano D, Paw UKT (1996) Surface renewal analysis for sensible and latent heat flux density. Boundary-Layer Meteorol 77:249–266

Spano D, Snyder RL, Duce P, Paw UKT (1997) Surface renewal analysis for sensible heat flux density using structure functions. Agric For Meteorol 86:259–271

Spano D, Snyder RL, Duce P, Paw UKT (2000) Estimating sensible and latent heat flux densities from gravepine canopies using surface renewal. Agric For Meteorol 104:171–183

Sparrow EM, Husar RB, Goldstein RJ (1970) Observations and other characteristics of thermals. J Fluid Mech 41:793–800

Tiselj I, Bergant R, Makov B, Bajsić I, Hestroni G (2001) DNS of turbulent heat transfer in channel flow with heat conduction in the solid wall. J Heat Transf 123:849–857

Townsend AA (1959) Temperature fluctuation over a heated horizontal surface. Fluid Mech 5:209–241

Vogt R (2008) Visualisation of turbulent exchange using a thermal camera. Paper no. 8B.1. 18th symposium on boundary layer and turbulence, Stockholm

Wilczak JM, Businger JA (1983) Thermally indirect motions in the convective atmospheric boundary layer. J Atmos Sci 40:343–358

Wilczak JM, Tillman JE (1980) The three-dimensional structure of convection in the atmospheric surface layer. J Atmos Sci 37:2424–2443

Wilczak JM, Oncley SP, Stage SA (2001) Sonic anemometer tilt correction algorithms. Boundary-Layer Meteorol 99:127–150

Wyngaard JC, Cote OR, Izumi Y (1971) Local free convection, similarity and the budgets of shear stress and heat flux. J Atmos Sci 28:1171–1182